

Chapter 1

Graphite and Intercalated Compound Superconductors: Atomic and Electronic Structures



Ritsuko Eguchi and Fumihiko Matsui

Abstract Graphite is a carbon allotrope with a unique anisotropy. The in-plane bonds of carbon have a strong covalent bonding characteristic, while out-of-plane bonding of carbon is due to the weak van der Waals interaction. Graphite can be easily exfoliated, i.e., a sheet of graphite called graphene can be easily separated. By intercalating metallic atoms, the property of graphite can be drastically altered. For example, CaC_6 is known as a graphite intercalation compound (GIC) superconductor having transition temperature of 11.5 K at ambient pressure. In the first half of this chapter, the brief history of GIC discovery as a superconducting material is outlined, and then the current understanding of GIC superconducting mechanism is described. In the second half of this chapter, the experimental verification of the atomic and electronic structures of the pristine graphite and GIC using photoelectron spectroscopy and diffraction is introduced. Finally, this chapter is summarized and expanded into future prospects.

Keywords Graphite · Intercalation · Photoelectron spectroscopy · Photoelectron diffraction

1.1 Introduction

Graphite is a carbon allotrope with a unique anisotropy. The in-plane bonds of carbon have a strong covalent bonding characteristic, namely, σ bonds due to sp^2 hybridization. A layer of honeycomb network structure is formed by sharing three

R. Eguchi (✉)
Okayama University, Okayama, Japan
e-mail: eguchi-r@okayama-u.ac.jp

F. Matsui
Institute for Molecular Science, Okazaki, Japan
Nara Institute of Science and Technology, Ikoma, Japan
e-mail: matui@ims.ac.jp

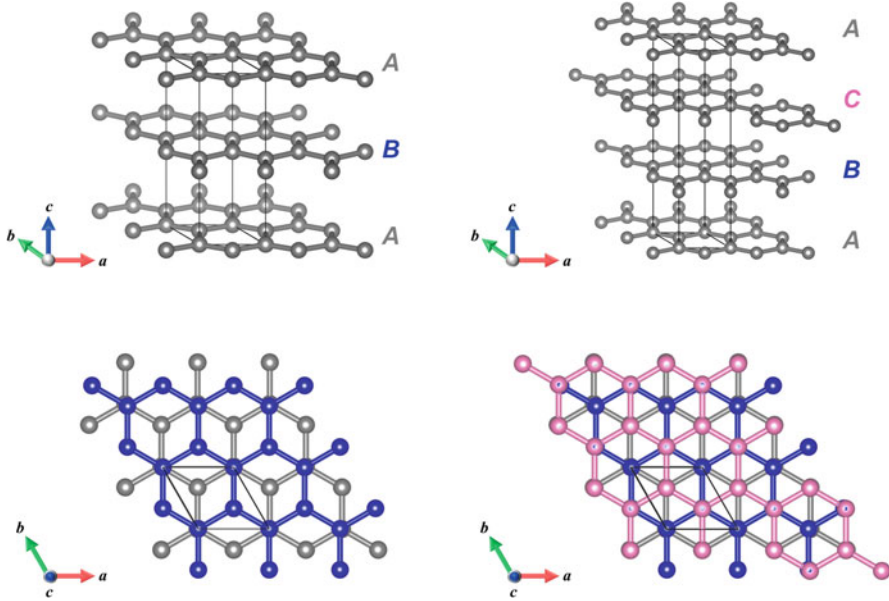
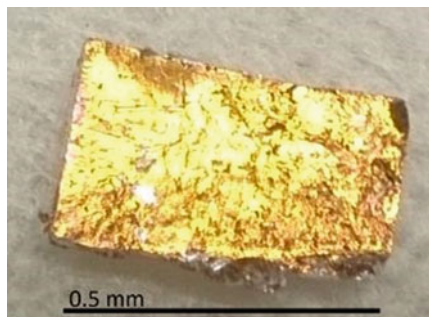


Fig. 1.1 Crystal structures of graphite stacked in *ABABAB* (left column) and *ABCABC* (right column) sequences. Hexagonal cell is shown in both crystal structures

sp^2 electrons of three adjacent carbons. The in-plane CC bond length is 1.421 Å. Moreover, the out-of-plane bonding of carbon is the result of the weak van der Waals interaction caused by delocalized π orbitals. The interplanar spacing of the carbon layer is about 3.35 Å. Graphite can be easily exfoliated, i.e., a sheet of graphite called graphene can be easily separated. The physical properties of graphene are explained in detail in Chap. 2. The carbon layer in graphite is stacked in two different forms, which are *AB* sequence (*ABABAB* ...) and *ABC* sequence (*ABCABC* ...), as shown in Fig. 1.1. The former is called α -graphite having a hexagonal structure, and the latter is called β -graphite having a rhombohedral structure. The hexagonal α -graphite is more stable than the rhombohedral β -graphite. In the case of α -graphite, there are tri-coordinated and penta-coordinated carbon atoms; however, in the case of β -graphite, only the tetra-coordinated carbon exists. A β -graphite can be converted to diamond without repositioning its bonds. The physical properties of diamond are described in detail in Chap. 3.

Graphite intercalation compounds (GIC) are old and new superconducting materials. Currently, the maximum transition temperature (T_c) value of a GIC superconductor (CaC_6) at ambient pressure is 11.5 K [1, 2]. Members of the GIC superconducting family have not changed for many years, except the T_c of BaC_6 , which was confirmed as 65 mK in 2015 [3]. Recently, a new series of bimetal-intercalated graphite superconductor, $\text{Ca}_x\text{K}_{1-x}\text{C}_y$, was successfully synthesized [4]. When K and Ca atoms are intercalated, graphite flakes turn into golden superconducting compounds (Fig. 1.2). This chapter focuses on the superconductivity

Fig. 1.2 Photograph of Ca- and K-intercalated graphite flake sample



of the GICs. In the first half of this chapter, the brief history of GIC discovery as a superconducting material is outlined, and then the current understanding of the GIC superconducting mechanism is described. In the second half of this chapter, the experimental verification of the atomic and electronic structures of the pristine graphite and GIC using photoelectron spectroscopy and diffraction is introduced. Finally, this chapter is summarized and expanded into future prospects.

1.2 Graphite Intercalation Compounds (GICs)

Over the years, GICs have attracted a considerable amount of attention from chemists and physicists due to their exciting electronic properties. In GICs, atoms and molecules are inserted into the space between the honeycomb carbon layers as intercalants. Intercalation provides a variation of many physical properties in graphite. Intercalated metals and molecules exist as intercalants of electron donor or acceptor type. This means that intercalation with different chemical species and concentrations may change the free carrier concentration in a graphite. As a result, GIC exhibits various electronic, thermal, and magnetic characteristics.

The synthesis of the first GIC, graphite sulfate, was reported by Schaffäutl in 1841 [5]. The systematic study of GICs began in the early 1930s, and “stage” was determined using X-ray diffraction techniques. Subsequently, its physical properties were systematically studied in the early 1940s. Since the discovery of GICs, comprehensive reviews of GICs have been reported: by Rüdorff in 1959 [6], Ebert in 1976 [7], H. Selig and L. B. Eber in 1980 [8], Ebert and Scanlon in 1980 [9], and Forsman et al. in 1983 [10]. A representative review of GICs was reported by M.S. Dresselhaus and G. Dresselhaus in 2002 [11]. GICs have been used as an anode material in batteries represented by the lithium-ion battery. Furthermore, superconductivity was observed in metal-intercalated graphite. In this chapter, based on the literature reported so far, we focused on the superconductivity of metal-intercalated graphite and its physical and chemical properties.

GICs possess a characteristic structure, in which atoms and molecules are inserted in the space between carbon layers. Another way of looking at the structure is to focus on the fact that one or several consecutive carbon layers are present

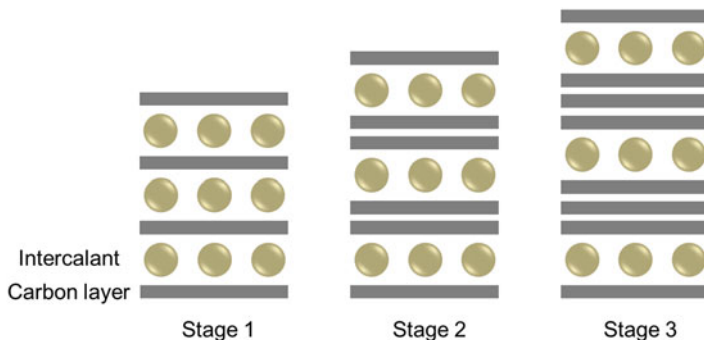


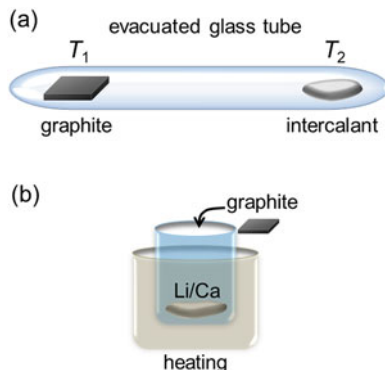
Fig. 1.3 Schematic represent of the different stages in GICs

between the intercalated atom layers. Depending on the number of consecutive carbon layers located in between the intercalated atom layers, the structural name of a GIC is defined. For example, the first stage (or stage 1) for one carbon layer, the second stage (or stage 2) for two carbon layers, and the third stage (or stage 3) for three carbon layers, and so on. Figure 1.3 shows a schematic diagram of the different stages in GICs.

As mentioned above, intercalated metals and molecules act as electron donor- or acceptor-type intercalants. Intercalants of the electron donor type are alkali and alkaline earth metals and rare earth metals (such as Li, Na, K, Cs, Ca, Sr, Ba, Sm, Eu, Yb, and Tm). Intercalants of the electron acceptor type are halogens, acids, and metal halides (such as Br_2 , ICl , IBr , AlCl_3 , FeCl_3 , CuCl_2 , SbCl_5 , MoCl_5 , AsF_5 , SbF_5 , HNO_3 , H_2SO_4 , H_3PO_4 , and HF) [11]. In addition to these representative binary and ternary (binary-element-intercalated) GICs, more complex materials are also reported. For a donor intercalant, liquid ammonia is used as a solvent for the intercalation of metals, such as Li, Na, K, Rb, Cs, Co, Sr, and Ba, to form a stoichiometric compound $\text{C}_{12}M(\text{NH}_3)_2$ ($M = \text{metals}$).

Various synthetic methods have been developed for the preparation of GICs, such as two-zone vapor transport technique (Fig. 1.4a), liquid intercalation method, and electrochemical method. To prepare a target material, various parameters, such as temperature, vapor pressure, gas, and reaction time, must be accurately controlled in each method. For metal-intercalated graphite exhibiting superconductivity, pioneers used vapor transport technique for synthesizing GICs. However, intercalation of alkaline earth metals into graphite has proven to be much more difficult than that of any alkali metals. For CaC_6 , vapor Ca reacts only on the surface region of graphite, and intercalation into graphite crystals is insufficient. This reduces the quality of the sample and does not show a sharp drop in magnetization at T_c and diamagnetic saturation. To overcome this problem, a new reaction method for graphite and metals has been developed. This reaction is carried out between pyrolytic graphite platelets and molten lithium-calcium alloy at about 350°C , under pure argon atmosphere (Fig. 1.4b) [1]. The reaction time can be between few days to 10 days. Despite

Fig. 1.4 (a) Two-zone vapor transport technique and (b) reaction technique using metal alloy



the lower Ca concentration compared to the Li content, Li is not present in the final reaction product, and Ca is homogeneously intercalated in the bulk graphite. The quality of the sample was improved using this method, showing a sharp drop in magnetization and a crystal structure of CaC_6 . Using this method with Ca/K/Li alloy, the synthesis of ternary GIC, $\text{Ca}_x\text{K}_{1-x}\text{C}_y$, became possible.

1.3 Superconductivity in GICs

In 1965, superconductivity of $T_c = 0.14$ K was observed in KC_8 , the interlayer K-intercalated graphite [12, 13], which is a stage 1 compound. This was the first observation of superconductivity in GICs. Note that, no superconductivity was observed in KC_{24} (stage 2), KC_{36} (stage 3), and KC_{48} (stage 4), suggesting that the alternating arrangement of metal and graphene layers (stage 1 structure) is important for superconductivity to occur in GICs. The K-intercalated graphite was prepared by heating highly purified K metal with highly oriented pyrolytic graphite (HOPG) in an evacuated tube. It was possible to obtain a gold compound as KC_8 . The magnetic susceptibility of KC_8 under a magnetic field $H//c$ exhibited type I characteristic, while that under $H\perp c$ exhibited type II characteristic [13], where c represents the perpendicular direction with respect to the carbon plane, as shown in Fig. 1.1. A KC_8 compound produced with stoichiometric amounts of the elements ($T_c = 0.39$ K) showed a higher anisotropy in the H_{c2} values, 25 Oe for a magnetic field $H\perp c$ and 250 Oe for $H//c$ [12]. A large variation in H_{c2} (H_c), as a function of magnetic field directions, was observed as a result of the anisotropy of mean free path, reflecting the two-dimensional (2D) crystal structure. Thus, the mean free path and the electrical conductivity in the carbon plane are much higher than those along the c axis. This anisotropy behavior was observed in other metal-intercalated graphite superconductors, such as CaC_6 , YbC_6 , and SrC_6 , which is described later.

Subsequently, the Rb- and Cs-intercalated graphite, RbC_8 and CsC_8 , were also discovered using an annealing synthesis method in the same manner as KC_8 ;

however, these GICs exhibited quite low T_c (less than 1 K) [12, 14, 15] like KC_8 [12, 13]. Furthermore, the high-pressure syntheses were successfully achieved in other metal intercalations, which increased the T_c up to 1.9 K at 33 kbar ($=0.33$ GPa) for LiC_2 [16], 5 K for NaC_2 [17], and 1.5–5.5 K for KC_3 , KC_4 , and KC_6 [17, 18]. These results imply that there are metastable phases, such as MC_2 or MC_3 , that are different from MC_8 (M : metal atom).

Moreover, ternary GICs, such as KHgC_8 (1.9 K) [19], RbHgC_8 (1.44 K) [19], $\text{KTl}_{1.5}\text{C}_4$ (2.7 K) [20], and $\text{CsBi}_{0.55}\text{C}_4$ (4.05 K) [21], were also synthesized. In these GICs, not only an electron transfer from intercalants to graphite but also a change in spacing between the graphite layers may affect superconductivity significantly. The spacing between graphite layers strongly depends on the T_c , which is described later. Thus, superconductivity of GICs was a significant research subject up to the late 1980s–early 1990s. However, in 1991, the discovery of metal-intercalated C_{60} fullerene compounds with higher T_c ($=18$ K) [22] drastically changed this situation and research on fullerene intercalated compounds attracted attention of many researchers.

In 2005, the discovery of superconductivity in CaC_6 ($T_c = 11.5$ K [1]) and YbC_6 ($T_c = 6.5$ K [2]) made a major breakthrough in the GIC research. CaC_6 provided the highest T_c ($=11.5$ K) among the GICs discovered so far. The T_c further increased under high pressure ($T_c = 15.1$ K at 7.5 GPa) [23]. The increase in T_c originated from a pressure-induced phonon softening related to an in-plane Ca phonon mode. Unfortunately, above 8 GPa, T_c suddenly decreased to 5 K, suggesting the occurrence of phase transition (probably a structural phase transition). After the discovery of superconductivity in CaC_6 and YbC_6 , the other alkaline earth metal (or alkaline earth plus alkali metal)-intercalated graphite, SrC_6 ($T_c = 1.65$ K) [24] and $\text{Li}_3\text{Ca}_2\text{C}_6$ ($T_c = 11.15$ K) [25], were also reported. Recently, a new GIC superconductor, BaC_6 ($T_c = 0.065$ K), was discovered [3], and the binary-element-intercalated graphite compounds, $\text{Ca}_x\text{K}_{1-x}\text{C}_y$ ($T_c \leq 11.5$ K), were synthesized [4]. Thus, the family of superconducting GICs has been well established; however, the no superconductors with T_c greater than 11.5 K have been reported yet.

The characteristic behaviors and parameters of GIC superconductors are exhibited in various experiments. The magnetization as a function of magnetic field, $M(H)$, of CaC_6 indicated clear critical points, H_{c1} and H_{c2} , which means that CaC_6 is a type II superconductor. H_{c2} was about 2500 Oe at 2 K with the magnetic field oriented along the c axis ($H_{c2}(\parallel c)$), while that measured with the magnetic field in the ab plane was about 7000 Oe ($H_{c2}(\perp c)$) [1]. Such anisotropy of the critical field was observed in YbC_6 and SrC_6 , where $H_{c2}(\perp c)/H_{c2}(\parallel c)$ (the anisotropy parameter) is approximately 2 [2, 24]. This anisotropy depends on the ratio of the electron masses along the two directions, $\parallel c$ and $\perp c$, which was followed by the Ginzburg-Landau theory. The value of the anisotropy parameter (2) was smaller than that for a pure graphite (7). This difference indicates that the band structure and Fermi surface are more three-dimensional (3D) in GIC superconductors as compared to those in pure graphite [2].

The crystal structure of KC_8 and RbC_8 shows the $\text{A}\alpha\text{A}\beta\text{A}\gamma\text{A}\delta\text{A}$ stacking along the c axis, which corresponds to the face-centered orthorhombic structure (space

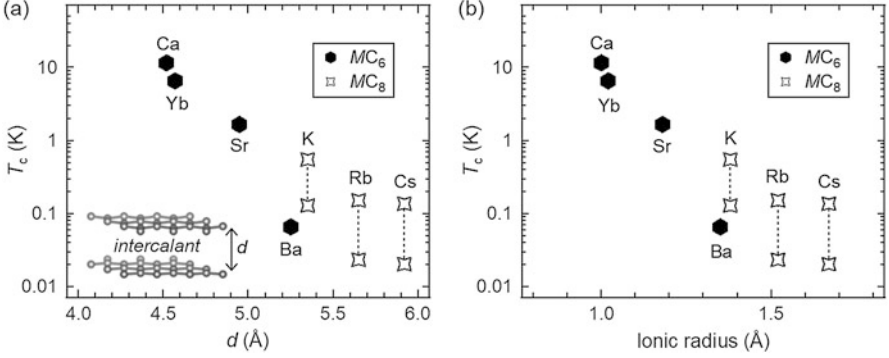


Fig. 1.5 Plots of T_c as a function of (a) d and (b) ionic radius in MC_6 (M : Ca [1, 2], Yb [2], Sr [24], and Ba [3]) and MC_8 (M : K [12, 13], Rb [12, 15], and Cs [12])

group: $Fddd$). Here, “A” refers to the honeycomb carbon layer, and “ α ,” “ β ,” “ γ ,” and “ δ ” refer to the metal layers (or different location) [14]. Moreover, the crystal structure of CaC_6 refers to the $A\alpha A\beta A\gamma A$ stacking (rhombohedral structure, space group; $R\bar{3}m$) [1]. The structures of YbC_6 [2], SrC_6 [26], and BaC_6 [3] correspond to the $A\alpha A\beta A$ stacking (hexagonal structure, space group: $P6_3/mmc$). The spacing, d , between the carbon layers increases depending on the size of intercalant atoms; the value of d is 4.52 Å for CaC_6 [1], 4.57 Å for YbC_6 [2], 4.95 Å for SrC_6 [24], 5.25 Å for BaC_6 [3], and 5.35 Å for KC_8 [11]. The value of T_c of GIC superconductors strongly depends on the value of d , indicating that the smaller d realizes GIC superconductors with higher T_c . Moreover, CaC_6 has the smallest value of d as compared to the other GICs, BaC_6 [3] and MC_8 (M : K, Rb, and Cs) [12–15], which have values of T_c less than 1 K; exceptionally T_c for YbC_6 is higher than 1 K [2]. The summary of T_c as a function of d is shown in Fig. 1.5a.

The highest T_c ($=15.1$ K) of Ca was realized at 7.5 GPa due to the further shrinkage of d [3, 24]. This is probably because the electron-phonon coupling sensitively changes against both in-plane intercalant and out-of-plane C phonon modes, resulting in the change of T_c [24], i.e., the small size of an intercalant decreases the d to produce high- T_c GIC. This relationship between T_c and ionic radius of the intercalants is also shown in Fig. 1.5b. The ionic radii are referred to M^{2+} ions for MC_6 and M^{1+} ions for MC_8 . The application of pressure to GIC can decrease the d value directly to realize a high- T_c GIC. As mentioned previously, the highest T_c of CaC_6 was achieved under the pressure of 7.5 GPa [23]. The T_c values varied with $dT_c/dP \sim 0.50$ K GPa $^{-1}$ in the pressure range of 0–1.2 GPa [27]. The KC_8 and SrC_6 compounds showed T_c of 1.7 K at 1.5 GPa [28] and 2 K at 1 GPa [24], respectively. The T_c value of SrC_6 increased with $dT_c/dP \sim 0.35$ K GPa $^{-1}$ [24]. In YbC_6 , T_c also increased with the applying pressure and reached the value of 7.1 K at 1.8 GPa with $dT_c/dP \sim 0.37$ K GPa $^{-1}$ [27]. Thus, all GIC superconductors showed pressure dependence similar to that of CaC_6 .

New superconducting $\text{Ca}_x\text{K}_{1-x}\text{C}_y$ compounds were successfully synthesized in 2016 [4]. These compounds were synthesized by immersing HOPG or Kish graphite in melted Li/K/Ca alloy (Fig. 1.4b). The T_c value of $\text{Ca}_x\text{K}_{1-x}\text{C}_y$ continuously increased with the increasing x , indicating the binary-element intercalation of Ca and K in graphite. Interestingly, the structure of $\text{Ca}_x\text{K}_{1-x}\text{C}_y$ ($0 \leq x \leq 0.6$) is the same as that of KC_8 , i.e., face-centered orthorhombic structure (space group: $Fddd$). Therefore, $\text{Ca}_x\text{K}_{1-x}\text{C}_y$ was represented as “ $\text{Ca}_x\text{K}_{1-x}\text{C}_8$ ” [4]. The d value of $\text{Ca}_x\text{K}_{1-x}\text{C}_8$ ($0 \leq x < 1$) was independent of x , which is nearly equal to one fourth of the lattice constant c (21.4 Å); $d = 5.35$ Å, which is enlarged as compared to that of CaC_6 (4.50 Å). The x independence of d ($x < 1$) suggested that the structure of $\text{Ca}_x\text{K}_{1-x}\text{C}_8$ was dominated by the K atom because of the larger ionic radius of K^+ (1.38 Å) than that of Ca^{2+} (1.00 Å).

The pressure dependence of resistance in $\text{Ca}_x\text{K}_{1-x}\text{C}_8$ ($x = 0.6$) was measured in a pressure range from 2.0 to 43 GPa [4]. A T_c value of 10.5 K was observed at 2.0 GPa. With more pressure, T_c increased and reached a maximum T_c value of 11.6 K at 3.3 GPa and then rapidly decreased to 4 K at 15 GPa. Thereafter, T_c slowly decreased, and no superconducting transition down to 1.9 K was observed at 43 GPa. This behavior is qualitatively similar to that observed for CaC_6 . The successful synthesis of superconducting binary-element-intercalated graphite may open a path for finding new graphite superconductors through a combination of various metals. Furthermore, details of the electronic and atomic structures for $\text{Ca}_x\text{K}_{1-x}\text{C}_y$ were elucidated by the photoelectron holography (PEH) technique, as discussed in Sect. 1.5 later. The 3D atomic arrangement around the intercalant atom was visualized, which provides a deeper understanding of the mechanism of superconductivity.

1.4 Superconducting Mechanism of GIC Superconductors

The physical properties of CaC_6 have been extensively studied to elucidate the superconducting mechanism because the highest T_c value of GICs was reported in CaC_6 under ambient and high pressure. The intercalants of alkali and alkaline earth metals provide electrons to the graphene layers in GICs, resulting in partially filled graphene π bands. In addition, the interlayer band, which is delocalized over the interstitial space of carbon layers, forms the free-electron-like Fermi surface. This interlayer band is hybridized with the π^* bands. This aspect is different from that of the simple electron doping of the π^* bands. The results of soft X-ray photoelectron spectroscopy suggested that not only the C $2p$ states but also the Ca $3d$ -derived states are located at the Fermi level [29]. The theoretical study suggested that the presence of the interlayer band was essential for stabilizing the superconductivity in GICs [30]. The interlayer band originated from the s band of the intercalant Ca. Thus, the interlayer band plays an important role for the superconductivity of GICs. The electron-phonon coupling, λ , due to the out-of-plane C phonon and in-plane Ca phonon was large enough to explain the relatively high T_c of GICs [31]. To experimentally elucidate the contribution of the Ca phonon to superconductivity,

the Ca isotope effect coefficient was reported in 2007 [32]. Based on the BCS theory [33], the isotopic effect shows that T_c depends on the mass of the nuclei, because a change in mass affects the lattice vibrations, which play an important role in the formation of the electron pairing in superconducting states. This means that it can indicate the phonon modes that are directly involved in the mechanism of superconductivity. The temperature-dependent magnetic susceptibility of CaC_6 synthesized using ^{40}Ca and ^{44}Ca clearly showed the shift in T_c , where a lower T_c was observed in ^{44}Ca intercalated graphite as compared to that of ^{40}Ca intercalated graphite. This result indicates that superconductivity is dominated by coupling of the electrons by the Ca phonon modes.

The superconducting mechanism of GICs is deeply debated based on the experimental and theoretical studies on superconducting CaC_6 . The result of the in-plane magnetic penetration depth suggested isotropic s -wave pairing, and the value of $2\Delta(0)/k_B T_c$ ($=3.6 \pm 0.2$) indicated a weakly coupled superconductor [34], where $2\Delta(0)$ and k_B are the superconducting gap and Boltzmann constant, respectively. Note that the BCS theory predicted the universal value of $2\Delta(0)/k_B T_c$, that is, 3.528. The specific heat measurements showed the anomaly characteristics of superconducting transition just at T_c , which indicates bulk superconductivity [35]. The temperature and magnetic dependence of electronic-specific heat provided a fully gapped superconducting parameter, namely, an isotropic s -wave BCS gap. The λ value of 0.70 ± 0.04 suggested that the high T_c of CaC_6 was explained by the intermediate coupling of the BCS scenario [35]. Scanning tunneling spectroscopy (STS) provided a clear superconducting gap in the quasiparticle density of states. An isotropic gap of $\Delta(0)$ was evaluated to be 1.6 ± 0.2 meV by fitting with the gap function of a conventional BCS theory, and $2\Delta(0)/k_B T_c = 3.66$ was slightly higher than the value expected in the weak coupling limit [36]. Furthermore, the presence of gap anisotropy was discussed, based on theoretical [37] and experimental [38] studies.

1.5 Atomic Structure of Graphite and GIC

1.5.1 Principle of Photoelectron Diffraction and New Holography Algorithm

To elucidate the mechanism of superconductivity, it is essential to directly visualize the 3D atomic arrangement around the intercalant atom. There are various types of approaches to atomic level structural analysis, such as X-ray diffraction, scanning transmission electron microscopy, and scanning probe microscopy. In this section, the PEH technique is described. When an atom is excited with X-ray, a photoelectron is emitted. Photoelectrons from localized core levels are excellent element-specific probes for atomic structure analysis. Due to the shallow probing depth of photoelectrons, PEH is a powerful method to study the local surface

and subsurface atomic structures in 3D. Information on the photoelectron-emitting atoms and the atomic arrangement around them is recorded as a photoelectron hologram in the photoelectron intensity angular distribution (PIAD). Forward focusing peaks (FFPs) at local interatomic directions [39–41] and diffraction rings around them appearing in the photoelectron hologram show the 3D atomic positions of the surrounding atoms with respect to the photoelectron-emitting atoms. A conventional reconstruction algorithm for PEH was based on the Fourier transform of the photoelectron hologram. However, the reconstructed image was greatly distorted by the effect of FFP without phase information. Recently, the scattering-pattern-extraction algorithm with maximum entropy method (SPEA-MEM), which is a new holographic algorithm for atomic arrangement reconstruction, was developed [42]. 3D images of atomic arrangements around the photoelectron-emitting atoms can be obtained directly from element-specific photoelectron holograms.

The photoelectron wave function in the case of a simple s -wave with kinetic energy E_k is expressed as an outgoing wave: $\Psi_0 = \exp(ikr)/r$. Wave number $k = \sqrt{2m_e E_k}/\hbar$ is the length of the wave vector \mathbf{k} . r is the distance from the excited atom. m_e is the mass of the electron. The photoelectron wave function Ψ_0 emitted from the atom is partially scattered by the surrounding N atoms, resulting in a scattered wave $\Psi^s = \sum_{i=1}^N \psi_i^s$. Consequently, interference occurs between the direct and scattered waves. We observe it as PIAD $I(\theta, \phi) = |\Psi_0 + \Psi^s|^2$.

Strictly speaking, the kinetic energy of the photoelectron E_k^{cryst} should be defined from the inner potential of the crystal, E_0 . The difference between E_k^{cryst} and E_k is $V_0 = E_0 + W$. The work function of the surface is represented by W . For graphite, V_0 is 17.17 eV. This value is obtained from the measurement value of the k_z band dispersion of the valence band, which is described later [43].

For example, a photoelectron scattering process with a 13-atom graphene cluster is simulated. Figure 1.6a shows the real part of the photoelectron wave function. The amplitude was rescaled by multiplying the distance r from the excited atom indicated by the central white circle. The kinetic energy of photoelectrons E_k was 500 eV. Figure 1.6b shows the variation in photoelectron intensity in real space $\chi(\mathbf{r}) = (I - \Psi_0^2)/\Psi_0^2$. The intensity of the photoelectron “tail” is formed at the position of the scatterer atom just like that in a comet. A photoelectron hologram $\chi(\theta, \phi)$ is an angular distribution measured by a detector located far from the sample. This photoelectron intensity tail is detected as FFP. Furthermore, if the phase difference between ψ_i^s and Ψ_0 is $2\pi n$ (n : integer number), the two waves constructively interfere and form diffraction rings around the FFP. Figure 1.6c shows the relationship between the atomic arrangement in real space and the hemispherical photoelectron hologram. The intensity of photoelectrons increases in the direction in which the diffraction rings overlap.

The measured C1s PIADs from graphite are shown in Fig. 1.7 [44]. A 2 mm diameter graphite single crystal was cleaved in air and mounted on a sample holder. The normal direction of the surface was aligned along the photon incident axis. The kinetic energies were (a) 500 eV and (b) 800 eV. Note that the diffraction ring arcs

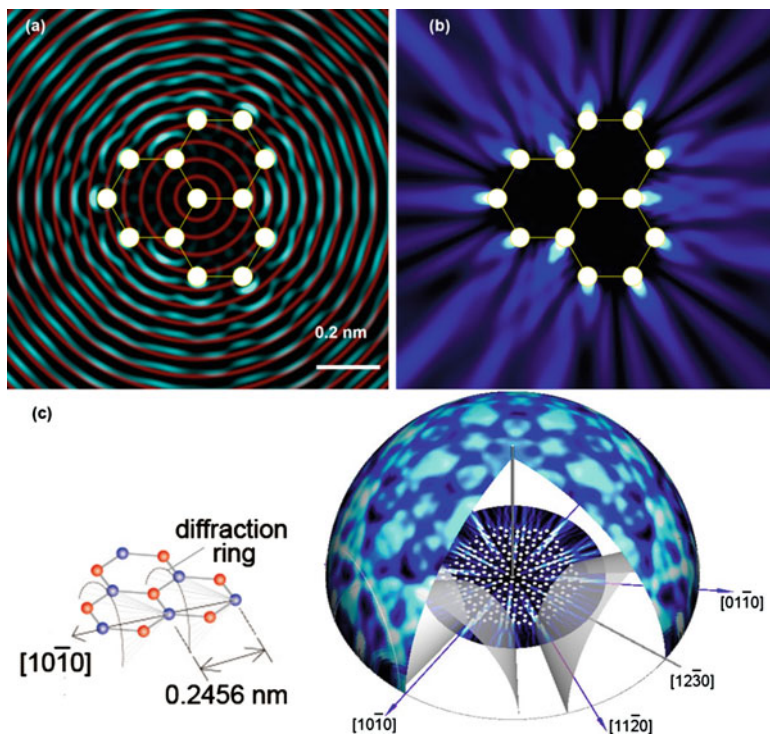


Fig. 1.6 (a) Real part of the photoelectron wave function from the central carbon atom in a C_{13} cluster, (b) photoelectron intensity in the real space $\chi(\mathbf{r})$, and (c) simulated photoelectron hologram $\chi(\theta, \phi)$ from a C_{253} graphene cluster

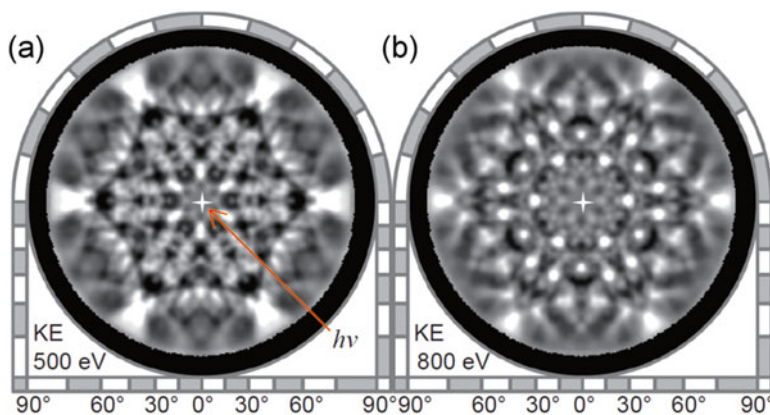


Fig. 1.7 C_{1s} photoelectron holograms from graphite. Kinetic energy was (a) 500 eV and (b) 800 eV [44]. (Copyright 2012 The Physical Society of Japan)

of the two PIADs have different radii corresponding to the different wave numbers of the photoelectrons.

The PEH reconstruction algorithm, SPEA-MEM, uses a fitting-based approach of diffraction rings and FFP with simulated data under maximum entropy method scheme [42]. In this case, the fitting of diffraction intensity oscillations as a function of the polar angle from the scatterer atom direction of the various CC atomic distances was applied to the entire set of the measurement data. As shown in Fig. 1.8, the real space images of several graphite layers above the photoelectron-emitting atom as well as the layers containing emitting atom were clearly reproduced [44]. The in-plane lattice vector and interlayer spacing of graphite were determined with an accuracy of 1% (Fig. 1.8a) and 3% (Fig. 1.8d), respectively. The atomic structure of graphite is shown in Fig. 1.9a. There are four types of atomic sites in the unit cell; thus, atomic images seen from each atomic site are superimposed. Note that some of the reconstructed spots are stronger. For the emitting atom layer image shown in Fig. 1.8a, the second nearest atomic image from the center emitting atom position appears brighter than the first nearest atomic image. This is because the atomic images from the two different sites overlap at the same position, as shown in Fig. 1.9b. Contrarily, for the atomic image of the upper layer shown in Fig. 1.8b, the first nearest atomic image appears more intense. The schematic diagram of Fig. 1.9c–i illustrates how different stacking structures result in modulation of reconstructed atomic image intensity. As shown in Fig. 1.9c–e, there are various types of graphene stacking structures. The “B” layer can be stacked on an “A” layer with a translational shift equal to the CC bond length in the CC bond direction shown in Fig. 1.9d, or the “B” layer can be stacked with a translational shift in the opposite direction, as shown in Fig. 1.9e. The stacked structure can be determined from the modulation of the atomic image contrast, as shown in Fig. 1.4f–i. For the layers stacked in the AA and AB sequences, the bright spots form triangular (Fig. 1.9f) and hexagonal (Fig. 1.9i) lattices, respectively.

The contrast modulation of the graphene lattice in one layer above (Fig. 1.8b) strongly indicates that the two adjacent layers are stacked in the AB sequence. In contrast, the contrast modulation of the graphene lattice in two layers above (Fig. 1.8c) indicates that the graphene layer is stacked in the same way as the emitting atom layer. Therefore, the reconstructed 3D atomic image shows that this graphite crystal has an ABAB (Bernal) stacking structure. Further, contrast modulation can be used to determine the in-plane and stacking structure of few-layered graphene [45] and GICs [46].

1.5.2 Atomic Arrangement Imaging of GIC Cleaved Surface

This PEH method was applied for the structural analysis of (Ca,K)C₈, superconductor ($T_c = 9.9$ K). The photoelectron spectra of the cleaved surface of (Ca, K)C₈ showed only the C 1s and K 2p peaks. The Ca 2p peak intensity was less than a few hundredths of the intensity of the K 2p peak. The observation of the K dominant

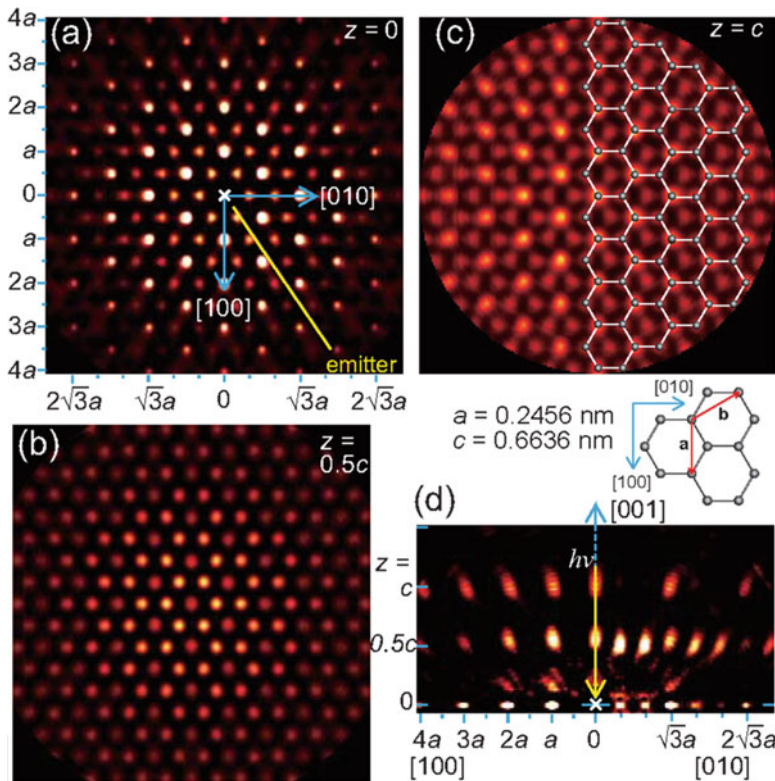


Fig. 1.8 Reconstructed atomic arrangement image of graphite from $C1s$ PD patterns [44]. The (a) graphite layer including the emitter atom, and the (b) first and (c) second layers above the emitter atom are shown. (d) Vertical cross sections of the real space images for the xz (left) and yz (right) planes. (Copyright 2012 The Physical Society of Japan)

structure on the cleaved surface means that the Ca atoms are dispersed in bulk and are likely to form high- T_c domains. Figure 1.10a, b shows the full hemisphere $C 1s$ and $K 2p$ photoelectron holograms with a kinetic energy of 600 eV [46]. The incident direction of the soft X-ray was aligned along the surface normal. From these holograms, the atomic image from the cleavage surface was directly reconstructed. Graphene atomic images were collected on the in-plane cross sections of layers 3.3 Å and 5.7 Å above the photoelectron-emitting C atoms, and the stacking structures were determined as AB and AA type, respectively. An intercalant metal atomic layer was observed between two AA -stacked graphenes, as shown in Fig. 1.10c, d. A K atomic image showing 2×2 periodicity, occupying each second central position of the C hexagonal prism, was reconstructed.

These results revealed that a preferential cleavage takes place in the K atom insertion layer without the Ca atoms. This is likely to be the most fragile part of the crystal samples. It is important to note that the cleavage planes do not necessarily represent the average bulk structure. The surface and bulk structures and

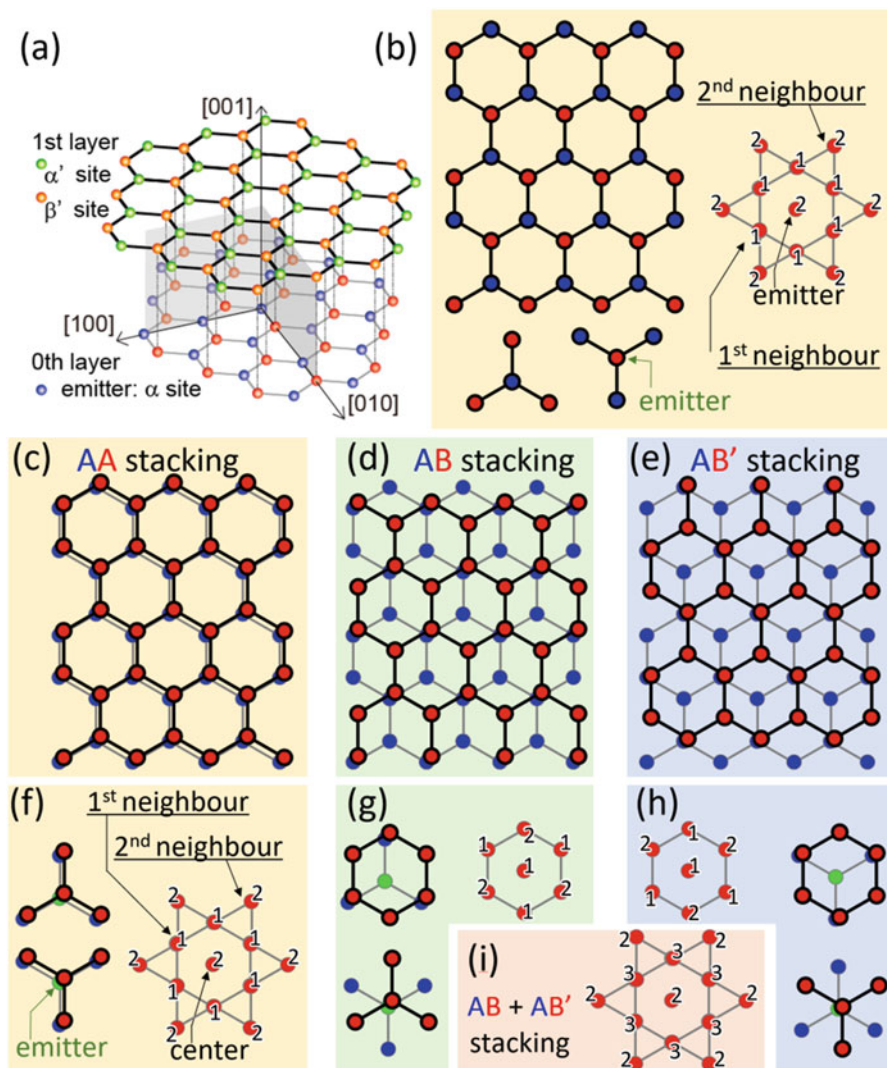


Fig. 1.9 (a) Graphite crystal model. Atomic configuration models of (b) emitter atom layer, (c) AA, (d) AB, and (e) AB' bilayer stacking structures. Graphene clusters can be stacked on top of the A graphene layer in three different ways. (f–i) The schematic structure model in each stacking geometry and the expected signal intensity ratio at the center; the first- and second-neighboring atoms in the reconstructed real space images

composition may be substantially different, especially in layered systems. Special precautions must be taken when using sensitive methods, such as ultraviolet angle-resolved photoelectron spectroscopy (ARPES) or scanning probe microscopy.

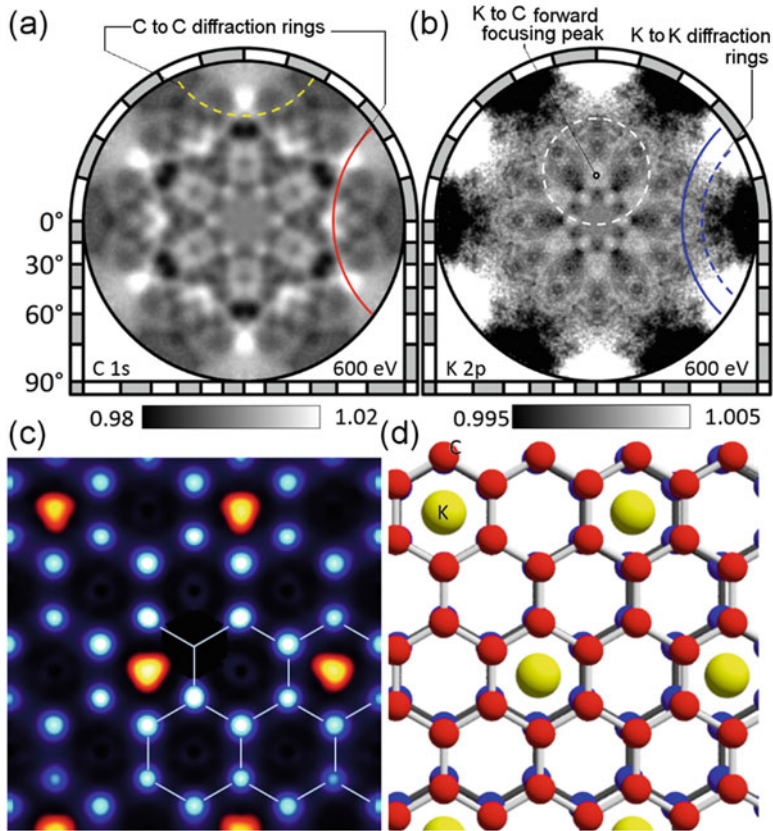


Fig. 1.10 (a) C 1 s and (b) K 2p photoelectron intensity angular distributions (holograms) from $(\text{Ca,K})\text{C}_y$. (c) Atomic arrangement image of C (blue) and K (orange) layers. (d) Structure model of the cleaved surface region of $(\text{Ca,K})\text{C}_y$ [46]. (Copyright 2016 The Author(s))

Surface phonons are often softened by bulk truncation, structural modification, and interaction with adsorbates. Recently, superconductivity of In [47] and Pb monoatomic layers [48] and FeSe ultrathin films [49] has been discovered and attracted substantial fundamental interest. As mentioned above, PEH is one of the most effective methods to study the surface and subsurface atomic structures in 3D. This method of directly visualizing the atomic arrangement by element selective PEH is expected to be a powerful tool for developing new superconducting materials.

1.6 Electronic Structure of Graphite and GIC

1.6.1 Transition Matrix Elements and Photoelectron Structure Factors

The electronic and chemical properties of a material are mainly determined by the movement of electrons near the Fermi level. The valence electron interaction and photoelectron interference are projected as PIAD patterns in momentum space. The valence band and core level photoelectron energy distribution curves reflect the density of states and compositions, respectively. Based on the principle of energy and momentum conservation in photoelectron emission process, photoelectron spectra resolved in all emission directions provide rich information on the atomic and electronic structures.

The ARPES of a valence band is a powerful technique to study such electrons. 2D Fermi surface mapping reveals the driving force of the electronic structure phase transition, such as charge density wave and superconductivity. Under higher kinetic energy conditions, the Brillouin zone appears within a small solid angle, where the transition matrix elements are approximately constant. 3D Fermi surfaces can be mapped using high angle-resolved electron spectrometer [50]. It is noteworthy that photoelectron spectroscopy using high photon energy probes the intrinsic bulk electronic states because of the long inelastic mean free path of the high kinetic energy electrons [51–53]. However, we encounter diffraction effects under higher kinetic energy conditions. In this chapter, the measurement of band dispersion by ARPES will be described. Furthermore, the photoelectron intensity variation among different Brillouin zones is discussed in detail.

Interlayer interactions induce the well-known degeneracy of the π band to two bands, a lower binding energy band π_L and a higher binding energy band π_H . In the photoelectron spectrum, the π_L and π_H bands appear alternately for each Brillouin zone along the \mathbf{k}_z direction. Consequently, oscillation of the binding energy as a function of the photon energy was observed at the bottom of the π band dispersion. This is explained by considering the constitutive and deconstructive interference of the p_z orbitals in the unit cell called the *photoelectron structure factor*. An analytical formula of the photoelectronic structure factor of graphite is shown.

We start with the transition matrix, M , between the initial and final states under the dipole approximation scheme. PIAD $I(\theta, \phi)$ is proportional to the square of M .

$$I(\theta, \phi) \propto D(E_B, \mathbf{q}) |M|^2 \delta_{E_f, h\nu + E_i} \delta_{\mathbf{k}, \mathbf{q} + \mathbf{G}}$$

$$M = \langle f | \mathbf{e} \cdot \mathbf{r} | i \rangle$$

$D(E_B, \mathbf{q})$ is the density of states in the Brillouin zone at binding energy E_B and at \mathbf{q} . The two delta functions ensure the law of energy and momentum conservation. Therefore, the relations $E_f = h\nu + E_i$ and $\mathbf{G} = \mathbf{k} - \mathbf{q} = \alpha\mathbf{a}^* + \beta\mathbf{b}^* + \gamma\mathbf{c}^*$ (α, β, γ : integer

numbers) hold for the primary photoelectron excitation process. The dipole operator $\mathbf{e} \cdot \mathbf{r}$ is expressed using spherical harmonics.

$$\mathbf{e} \cdot \mathbf{r} = \sum_{\sigma=-1}^1 \sqrt{\frac{4\pi}{3}} e_{\sigma} Y_{1\sigma}(\theta, \phi)$$

For $\sigma = 1$ helicity, $e_1 = 1$, $e_0 = 0$, and $e_{-1} = 0$. For x -polarization, $e_{\pm 1} = \mp 1/\sqrt{2}$ and $e_0 = 0$.

The initial state $|i\rangle$ with the wave vector \mathbf{q} and energy E_i is written by a Bloch state in tight-binding approximation as

$$|i\rangle = \frac{1}{\sqrt{N}} \sum_j \sum_{nv} e^{i\mathbf{q} \cdot \mathbf{R}'_j} u_{nv}(\mathbf{q}) \varphi_{nv}(\mathbf{r} - \mathbf{R}'_j),$$

$$\mathbf{R}'_j \equiv R_j + \tau_n,$$

where N is the total number of atoms and \mathbf{R}'_j is the position vector of the n th atom at τ_n in the j th unit cell at R_j . $\varphi_{nv}(\mathbf{r})$ is the ν th orbital of the n th atom, which is the product of a radial function $R_{nl}(r)$ and a spherical harmonics $Y_{lm}(\theta, \phi)$. $u_{nv}(\mathbf{q})$ is its LCAO coefficient. The final state $|f\rangle$ with the wave vector \mathbf{k} and energy E_f is also a Bloch state in bulk and is written as

$$|f\rangle = 4\pi \sum_{l'm'} i^{l'} e^{-i\delta_{l'}} Y_{l'm'}^*(\theta_k, \phi_k) Y_{l'm'}(\theta, \phi) R_{E_f, l'}(r).$$

Using the above equations for the initial and final states, a formula for the matrix elements is derived. $\mathbf{G} = \mathbf{k} - \mathbf{q}$ is a reciprocal vector.

$$\begin{aligned} M &= \frac{1}{\sqrt{N}} \sum_j \sum_{nv} e^{-i(\mathbf{k}-\mathbf{q}) \cdot \mathbf{R}'_j} u_{nv}(\mathbf{q}) A_{nv} \\ &= \sum_{nv} \exp(-i\mathbf{G} \cdot \tau_n) u_{nv}(\mathbf{q}) A_{nv} \end{aligned}$$

where the ‘‘angular distribution from atomic orbital ADAO’’ A_{nv} is defined as follows [54]:

$$A_{nv} \equiv \langle f(\mathbf{r}) | \mathbf{e} \cdot \mathbf{r} | \varphi(\mathbf{r}) \rangle = \sum_{l'=1\pm 1} R_{l'} \sum_{m'} e_{\sigma} Y_{l'm'}(\theta_k, \phi_k) c^1(l', m', l, m)$$

$$\sigma = m' - m$$

$R_{l'}$ is the radial part of the transition matrix element and is a constant complex number depending on l , l' , and photon energy. The Gaunt coefficient $c^1(l', m', l, m)$ is nonzero only when $\sigma = \pm 1$ or 0.

If the initial state consists of only one type of atomic orbital, the ADAO term can be separated out of the absolute value as

$$|M|^2 = \left| \sum_n \exp(-i\mathbf{G} \cdot \boldsymbol{\tau}_n) u_n(\mathbf{q}) \right|^2 |A(\theta, \phi)|^2 = |F(\mathbf{k})|^2 |A(\theta, \phi)|^2.$$

where “photoemission structure factor PSF” $F(\mathbf{k})$ [55] is introduced as

$$F(\mathbf{k}) = \sum_n \exp(-i\mathbf{G} \cdot \boldsymbol{\tau}_n) u_n(\mathbf{q}).$$

The term $|F|^2$ is the intensity distribution in the reciprocal \mathbf{k} space independent of the kinetic energy of photoelectrons or the angle of incidence of photons. This factor is derived from the interference of photoelectron waves from different groups of atoms in the unit cell and is similar to the structural factor of X-ray or electron diffraction that replaces the scattering factors by the coefficient of each atomic orbit in the LCAO wave function [56]. The PIAD from the valence band can be understood as the product of the band dispersion, PSF, and ADAO in simple cases. In the following description, it is shown how these terms work on the actual systems using single-crystal graphite data.

There are four carbon atoms in the unit cell of a graphite. The intralayer bond of carbon has strong covalent properties, i.e., σ bonds with sp^2 hybridization. The layer of the honeycomb network structure is formed by sharing three sp^2 electrons of three adjacent carbon atoms. Moreover, the interlayer bond of carbon is caused by the weak van der Waals interactions produced by delocalized π orbitals. As shown in Figs. 1.1 and 1.11a, there are three- and five-coordinated carbon atoms in the Bernal stacked structure.

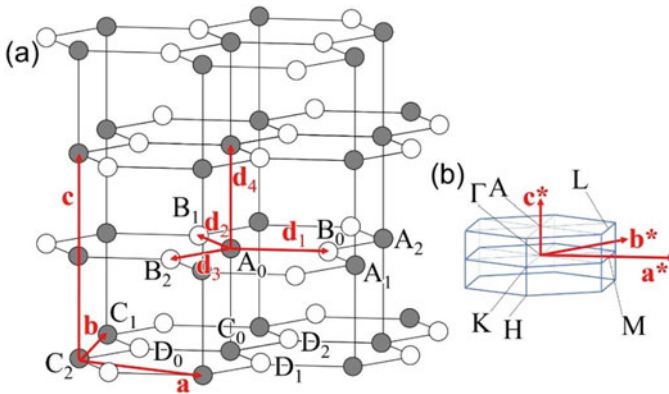


Fig. 1.11 (a) Graphite atomic structure and (b) Brillouin zone

The four C $2p_z$ orbitals p_A , p_B , p_C , and p_D , in the unit cell form the π band dispersions. The wave function of the π band $\varphi(\mathbf{q}, \mathbf{r})$ is as follows:

$$\begin{aligned}\varphi(\mathbf{q}, \mathbf{r}) &= \frac{1}{\sqrt{N}} \sum_n e^{i\mathbf{q}\cdot\mathbf{r}_{A_n}} u_A p_A + e^{i\mathbf{q}\cdot\mathbf{r}_{B_n}} u_B p_B + e^{i\mathbf{q}\cdot\mathbf{r}_{C_n}} u_C p_C + e^{i\mathbf{q}\cdot\mathbf{r}_{D_n}} u_D p_D \\ &= \frac{1}{\sqrt{N}} \sum_n e^{i\mathbf{q}\cdot\mathbf{R}_n} \left[e^{i\mathbf{q}\cdot\mathbf{d}_4/2} (u_A p_A + e^{i\mathbf{q}\cdot\mathbf{d}_1} u_B p_B) \right. \\ &\quad \left. + e^{-i\mathbf{q}\cdot\mathbf{d}_4/2} (u_C p_C + e^{-i\mathbf{q}\cdot\mathbf{d}_1} u_D p_D) \right]\end{aligned}$$

\mathbf{d}_1 , \mathbf{d}_2 , \mathbf{d}_3 , and \mathbf{d}_4 are the position vectors of the neighboring C atoms. The in-plane and interlayer phase factors are introduced as follows:

$$g(\mathbf{q}) = e^{i\mathbf{q}\cdot\mathbf{d}_1} + e^{i\mathbf{q}\cdot\mathbf{d}_2} + e^{i\mathbf{q}\cdot\mathbf{d}_3}$$

$$h(\mathbf{q}) = e^{i\mathbf{q}\cdot\mathbf{d}_4} + e^{-i\mathbf{q}\cdot\mathbf{d}_4} = 2 \cos \mathbf{q} \cdot \mathbf{d}_4$$

The matrix elements $H_{ij} = \langle p_i | H | p_j \rangle$ are classified as follows: Coulomb integrals, $H_{ii} = \varepsilon_p$, and resonance integrals between two p orbitals, $H_{AB} = H_{CD} = -V_{pp\pi}$ and $H_{AC} = V_{pp\sigma}$. The secular equation is

$$\begin{pmatrix} \varepsilon_p - E & V_{pp\pi} g & V_{pp\sigma} h & 0 \\ V_{pp\pi} g^* & \varepsilon_p - E & 0 & 0 \\ V_{pp\sigma} h & 0 & \varepsilon_p - E & V_{pp\pi} g^* \\ 0 & 0 & V_{pp\pi} g & \varepsilon_p - E \end{pmatrix} \begin{pmatrix} u_A \\ u_B \\ u_C \\ u_D \end{pmatrix} = 0$$

which leads to

$$E_{\pi_L} = \varepsilon_p - \frac{1}{2} \sqrt{(2V_{pp\pi} |g|)^2 + (V_{pp\sigma} |h|)^2} - \frac{V_{pp\sigma} |h|}{2}$$

$$E_{\pi_H} = \varepsilon_p - \frac{1}{2} \sqrt{(2V_{pp\pi} |g|)^2 + (V_{pp\sigma} |h|)^2} + \frac{V_{pp\sigma} |h|}{2}$$

$$E_{\pi_L^*} = \varepsilon_p + \frac{1}{2} \sqrt{(2V_{pp\pi} |g|)^2 + (V_{pp\sigma} |h|)^2} - \frac{V_{pp\sigma} |h|}{2}$$

and

$$E_{\pi_H^*} = \varepsilon_p + \frac{1}{2} \sqrt{(2V_{pp\pi} |g|)^2 + (V_{pp\sigma} |h|)^2} + \frac{V_{pp\sigma} |h|}{2}.$$

Note that $\varepsilon_p \mp \sqrt{(2V_{pp\pi} |g|)^2 + (V_{pp\sigma} |h|)^2}/2$ corresponds to the binding energy of the π (-) and π^* (+) band dispersions, for graphene. The third term $\mp V_{pp\sigma} |h|/2$ represents the further degeneration of the π (-) and π^* (+) bands. The LCAO

coefficients for the π bands (π_H and π_L) are as follows. $u_A = \pm u_C \propto \varepsilon_p - E$, $u_B \propto V_{pp\pi} g^*$, and $u_D \propto \pm V_{pp\pi} g$. $u_A^2 + u_B^2 + u_C^2 + u_D^2 = 1$. The following equation is for the PSF of the π band. The plus and minus signs correspond to the H and L bands, respectively.

$$F = e^{-i\mathbf{G}\cdot\mathbf{d}_4/2} \left(u_A + e^{-i\mathbf{q}\cdot\mathbf{d}_1} u_B \right) \pm e^{i\mathbf{G}\cdot\mathbf{d}_4/2} \left(u_C + e^{i\mathbf{q}\cdot\mathbf{d}_1} u_D \right)$$

Finally, the PSF formula for graphite Brillouin zone is obtained [43]. Note that $\mathbf{G} \cdot \mathbf{d}_1 = 2\pi(2\alpha + \beta)/3$ and $\mathbf{G} \cdot \mathbf{d}_4 = \pi\gamma$. For the even Brillouin zone along the k_z direction ($\gamma=2n$)

$$|F_{\pi_L}|^2 = \frac{2}{(\varepsilon_p - E_{\pi_L})^2 + V_{pp\pi}^2 g g^*} \left[V_{pp\pi} \sum_{x=1}^3 \sin(\mathbf{G} \cdot \mathbf{d}_1 + \mathbf{q} \cdot \mathbf{d}_x) \right]^2$$

$$|F_{\pi_H}|^2 = \frac{2}{(\varepsilon_p - E_{\pi_H})^2 + V_{pp\pi}^2 g g^*} \left[\varepsilon_p - E_{\pi_H} - V_{pp\pi} \sum_{x=1}^3 \cos(\mathbf{G} \cdot \mathbf{d}_1 + \mathbf{q} \cdot \mathbf{d}_x) \right]^2.$$

For the odd Brillouin zone along the k_z direction ($\gamma=2n + 1$):

$$|F_{\pi_L}|^2 = \frac{2}{(\varepsilon_p - E_{\pi_L})^2 + V_{pp\pi}^2 g g^*} \left[\varepsilon_p - E_{\pi_L} - V_{pp\pi} \sum_{x=1}^3 \cos(\mathbf{G} \cdot \mathbf{d}_1 + \mathbf{q} \cdot \mathbf{d}_x) \right]^2,$$

$$|F_{\pi_H}|^2 = \frac{2}{(\varepsilon_p - E_{\pi_H})^2 + V_{pp\pi}^2 g g^*} \left[V_{pp\pi} \sum_{x=1}^3 \sin(\mathbf{G} \cdot \mathbf{d}_1 + \mathbf{q} \cdot \mathbf{d}_x) \right]^2.$$

Figure 1.12a, b shows the structure factor for the π_H and π_L bands, respectively. The C $2p_z$ atomic orbitals at Γ for the π_H and π_L bands are depicted together as Fig. 1.12c, d, respectively. Note that the p_z orbitals in the π_L band (bonding) are aligned to be in antiphase, and the p_z orbitals in the π_H band (anti-bonding) are aligned to have the same phase. The alignment of these π_L and π_H bands produces destructive and constructive interference, respectively, in the first Brillouin zone and vice versa in the second Brillouin zone.

The cross sections of the valence band dispersion of graphite close to the plane of symmetry of HAH and LAL are shown in Fig. 1.13. The photon energy was set and maintained at 80 eV. The analyzer was set and maintained at 60° off from the incident light. The acceptance angle mode of the analyzer was $\pm 30^\circ$ perpendicular to the plane containing the incident light, its electric vector, and the direction to the center of the analyzer entrance slit. The valence band consists of one π band and three σ bands. A schematic 3D band dispersion is shown in Fig. 1.13b. The red, yellow, green, and blue bands correspond to π , σ_3 , σ_2 , and σ_1 (or $2s$) band, respectively. The π band from the Fermi level to the binding energy of 8 eV consists

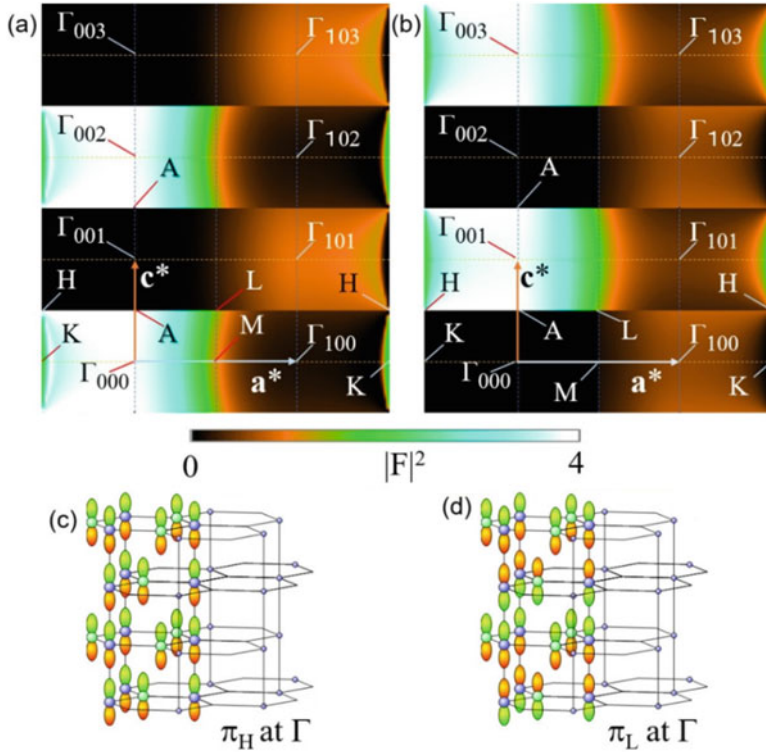


Fig. 1.12 Square of structure factors (PSF), $|F|^2$, for (a) π_H band and (b) π_L band. The color scale indicates the PSF intensity with white and black corresponding to 1 and 0, respectively. C $2p_z$ atomic orbitals at Γ for (c) π_H and (d) π_L bands [43]. (Reprinted with permission from [43]. Copyright 2018 American Physical Society)

of a C $2p_z$ orbital. Two σ bands from about 5–12 eV are made from the C $2p_x$ and $2p_y$ orbitals. The σ_1 band of 12–20 eV is mainly from the C $2s$ orbitals.

The left and center columns of Fig. 1.14 are the PIADs of graphite obtained using He II (40.8 eV) and linearly polarized synchrotron radiation, respectively. In the latter case, the photon energy was adjusted to 45.2 eV to suppress the influence of Umklapp scattering. The brightness is proportional to the photoelectron intensity. The graphite has honeycomb carbon sheets, whose electronic structure exhibits sixfold symmetry. The hexagon in Fig. 1.14 represents the first Brillouin zone of graphite. As shown in Fig. 1.14i, the center of the hexagon is the Γ/A point, the vertex is the K/H point, and the midpoint of one side is the M/L point.

The photoelectrons at the Fermi level shown in Fig. 1.14a, e are from the vicinity of the H points, where the π bands degenerate. In the case of non-polarized light excitation, all six points are bright; however, only four points are observed in the case of linearly polarized light excitation. This is due to the characteristic of p_z ADAO, as shown in Fig. 1.14l.

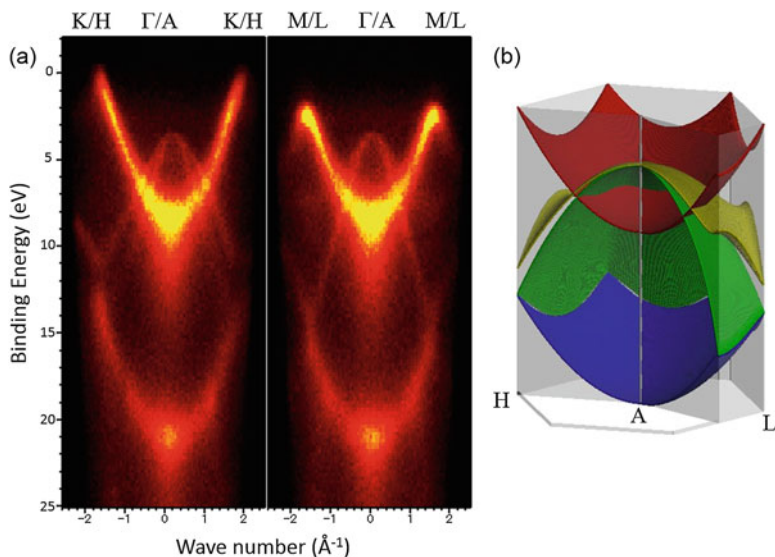


Fig. 1.13 (a) Valence band dispersion of graphite along the $K\Gamma MK/HALH$ symmetry plane. The photon energy was 80 eV. (b) 3D band diagram of graphite at the HALH plane

As the binding energy increases to 2.0 eV, the π band is dispersed to the M/L points. Although six M points appear to be bright, the outside region of the M point of the second Brillouin region remains dark. This is explained by the PSF of the π band shown in Fig. 1.14i. The photoelectron intensity along the KM/HL line outside the first Brillouin region is calculated as zero, which is consistent with the experimental observations. This intensity inequality between the first and second Brillouin zones means that this π band is a “same-phase (bonding) band.”

A σ band appears at the Γ/A point with the binding energy of 4.0 eV. The π band appearing as a ring-shaped feature is dispersed to the Γ/A point, and the σ band is dispersed toward the M/L points. As shown in Fig. 1.14h, for linearly polarized light, note that the σ band intensity is observed only at the four M/L points. This indicates that the σ band is composed of the p_x and p_y atomic orbitals.

The overall characteristics of the intensity distribution are determined by the ADAO, A_v , and modified by the PSF. The PIAD measurements, along with the combination of a display-type analyzer and linearly polarized light, allow the analysis of atomic orbitals and bonding characters. From A_v , it is possible to determine the atomic orbital that forms the bands, and the bonding nature can be determined from the PSF. In other words, phase relations between the atomic orbitals in the unit cell can be deduced [43, 55, 56, 57].

The valence band dispersion of the graphite π band along the \mathbf{k}_z axis was measured using the photon energy of 60–230 eV. The oscillation in binding energy was observed for π band dispersion during photon energy scanning. The binding

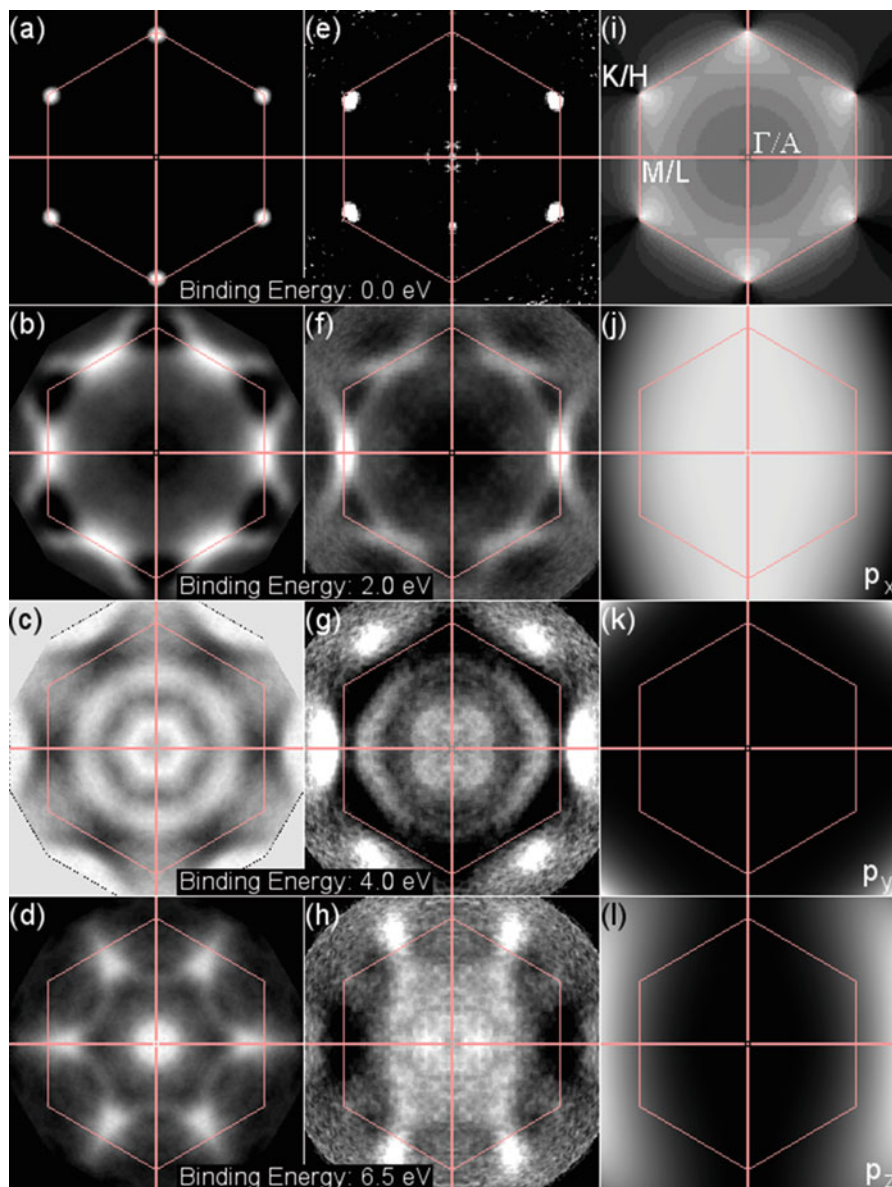


Fig. 1.14 (a–d) PIADs of graphite excited by the He II (40.8 eV) radiation. The hexagon represents the Brillouin zone. (e–h) PIADs excited by the linearly polarized synchrotron radiation (45.2 eV). The electric vector is along the horizontal direction. (i) Structure factor of the graphite π band. ADAO from (j) p_x , (k) p_y , and (l) p_z atomic orbitals calculated for the photoelectron kinetic energy of 36 eV

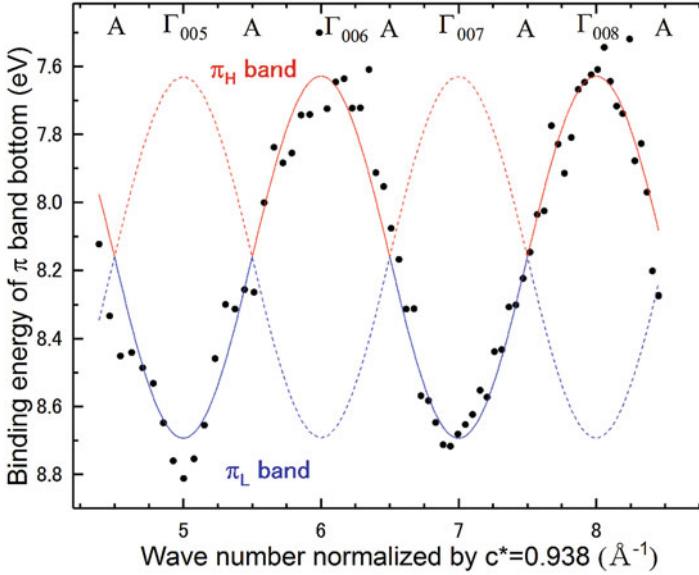


Fig. 1.15 Graphite band dispersion measured at Γ/A as a function of the photon energy. Binding energy at the bottom of the π band dispersion plotted as a function of wave number [43] (Reprinted with permission from [43]. Copyright 2018 American Physical Society)

energy at the bottom of the π band, as a function of photon energy, is plotted in Fig. 1.15. The horizontal axis is the wave number normalized by the reciprocal lattice c^* . The integer positions correspond to the Γ points. Considering the inner potential as a fitting parameter, the kinetic energy of each data point was converted into wave number so that the minimum and maximum values appear at Γ point.

At odd number points, the binding energy at the bottom of the π band is low. At even number points, the binding energy is high. The former corresponds to the π_L band. The latter corresponds to the π_H band. This oscillation is well explained by the PSF effect in the k_z direction, as shown in Fig. 1.12a, b. The π_L band is formed by the p_z orbitals that are in antiphase with each other forming destructive interference at $k_z = 2nc^* \Gamma$ points. The π_H band is formed by the p_z orbitals aligned in the same phase forming constructive interference at $k_z = 2nc^* \Gamma$ points. Thus, the PSF effect leads to complete disappearance of one π band and a 4 π band dispersion.

Fitting was done by finding the position of Γ points using a simple sine curve. From this fitting, the resonance integral between the interlayer p_z orbitals, $V_{pp\sigma}$ was derived as 0.5 eV. Furthermore, the inner potential of the graphite from the vacuum level was determined to be 17.17 eV. This value roughly corresponds to the midpoint between the bottom of π and σ bands at the Γ point.

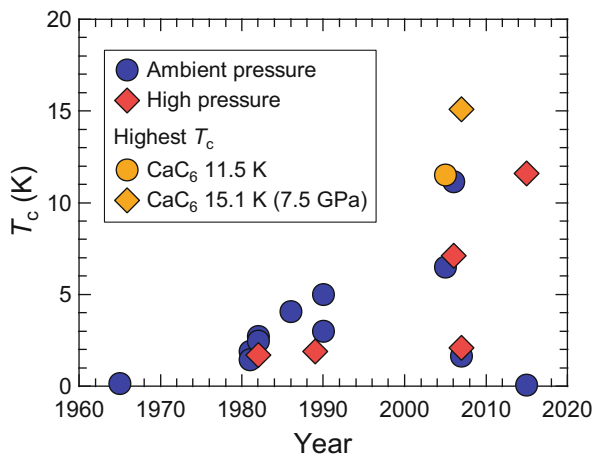
1.6.2 Valence Band Dispersion of GIC

The details of the electronic structures of CaC_6 were clarified by the ARPES experiment. ARPES is a powerful technique to experimentally determine the band dispersion of the valence band and Fermi surfaces. Details of ARPES are given in Sect. 1.6.1. The ARPES study of CaC_6 was reported in 2009 [58]. Its results suggested that the graphene sheet plays an important role in GIC superconductivity and no interlayer bands are observed. The electron-phonon coupling on the Fermi surface, derived from the π^* band, was strong and anisotropic. Moreover, Sugawara et al. reported that a small electron pocket derived from the π^* band appears near the Fermi level at the K point [59]. The triangular Fermi surface at the K point was formed in the π^* band, and almost no opening of the superconducting gap was observed. This result was explained by the simple rigid band shift by electron doping. In addition, they pointed out that an extra structure at the Γ point was observed. Neither a simple rigid band shift nor the π^* band, folding due to the superstructure of the Ca intercalant, explained this observation [59]. It was suggested that the free-electron-like spherical Fermi surface observed at point Γ is due to the interlayer coupling of CaC_6 . The superconducting gap was estimated to be between 1.8 ± 0.2 – 2.0 ± 0.2 meV at different momentum points around the Γ point, and $2\Delta(0)/k_B T_c$ was determined to be 4.1 ± 0.5 [59], indicating an intermediate or strong coupling regime. Two superconducting gaps of $\Delta E_{\pi^*} = 0.5 \pm 0.1$ meV and $\Delta E_{\text{IL}} = 0.4 \pm 0.1$ meV are present in both π^* and the intermediate layer [60]; thus, it was suggested recently that both bands are involved in superconductivity. Therefore, although the electronic structure is still being studied, the ARPES research at high energy resolution can provide the electronic structure of the GIC superconductor to clarify the origin of superconductivity.

1.7 Future Perspectives of GIC Superconductor

The most critical problem in the research of GIC superconductors is that the materials exhibiting T_c higher than 11.5 K found for CaC_6 [1, 2] have never been synthesized in the past decade. Figure 1.16 shows the evolution of transition temperatures T_c in GIC superconductors [61]. The trial for designing new GIC with higher T_c through intercalation of single element has always failed. As described in Sect. 1.3, the binary-element-intercalated graphite (the ternary GICs) compounds were successfully synthesized in the late 1980s, and new GICs have been discovered in recent years, e.g., $\text{Ca}_x\text{K}_{1-x}\text{C}_y$ ($x = 0.33$ – 0.7). Their structure and pressure dependence of superconductivity were fully investigated [4], and this study expanded the viewpoint of the GIC research to design new GIC compounds. Although T_c did not exceed 15.1 K for CaC_6 at 7.5 GPa, the intercalation of binary or ternary elements may be effective to enhance the GIC superconductors.

Fig. 1.16 Evolution of transition temperatures (T_c) in GIC superconductors



The strategy for realizing a higher T_c than 11.5 K at ambient pressure (or 15.1 K at high pressure) is still unclear. However, the recent discovery of superconductivity in graphene may become a key for realizing higher T_c in GICs. Moreover, the surface region of GIC may have different superconducting phases from those of bulk crystals. If the superconducting phase in the confined region can be selectively detected, this region may be utilized for electronic devices. The techniques of scanning tunneling spectroscopy (STS), conduction atomic force microscopy (AFM), and magnetic force microscopy (MFM) may be available for detecting superconducting phase in the surface region. As described in Sect. 1.5, the PEH of $\text{Ca}_{0.6}\text{K}_{0.4}\text{C}_8$ was successfully measured to clarify its surface structure [46]. The PEH method is effective to clarify the surface structure of the GIC superconductors, implying that the superconducting phase structure in the surface region can be determined as well. The microprobe and holography techniques may enable the detection and utilization of high- T_c superconducting phase appeared only in the confined region different from bulk superconductivity. Part of Sects. 1.3, 1.4, and 1.6.2 refers to [61] (Copyright 2016 IOP publishing).

References

1. N. Emery, C. Hérold, M. d'Astuto, V. Garcia, C. Bellin, J.F. Maréché, P. Lagrange, G. Loupiau, *Phys. Rev. Lett.* **95**, 087003 (2005)
2. T.E. Weller, M. Ellerby, S.S. Saxena, R.P. Smith, N.T. Skipper, *Nat. Phys.* **1**, 39–41 (2005)
3. S. Heguri, N. Kawade, T. Fujisawa, A. Yamaguchi, A. Sumiyama, K. Tanigaki, M. Kobayashi, *Phys. Rev. Lett.* **114**, 247201 (2015)
4. H.T.L. Nguyen, S. Nishiyama, M. Izumi, L. Zheng, X. Miao, Y. Sakai, H. Goto, N. Hirano, Y. Oishi, T. Kagayama, K. Shimizu, Y. Kubozono, *Carbon* **100**, 641–646 (2016)
5. P. Schaffäitl, *J. Prakt. Chem.* **21**, 155 (1841)
6. W. Rüdorff, *Adv. Inorg. Chem. Radiochem.* **1**, 223 (1959)

7. L.B. Ebert, *Annu. Rev. Mater. Sci.* **6**, 181–211 (1976)
8. H. Selig, L.B. Ebert, *Adv. Inorg. Chem. Radiochem* **23**, 281–327 (1980)
9. L.B. Ebert, J.C. Scanlon, *Ind. Eng. Chem. Prod. Res. Dev.* **19**, 103 (1980)
10. W.C. Forsman, T. Dziemianowicz, K. Leong, D. Carl, *Synth. Met.* **5**, 77–100 (1983)
11. M.S. Dresselhaus, G. Dresselhaus, *Adv. Phys.* **51**, 1–186 (2002)
12. N.B. Hannay, T.H. Geballe, B.T. Matthias, K. Andres, P. Schmidt, D. MacNair, *Phys. Rev. Lett.* **14**, 225–226 (1965)
13. Y. Koike, H. Suematsu, K. Higuchi, S. Tanuma, *Solid State Commun.* **27**, 623–627 (1978)
14. A. Hérold, D. Billaud, D. Guérard, P. Lagrange, M.E. Makrini, *Physica B* **105**, 253–260 (1981)
15. M. Kobayashi, T. Enoki, H. Inokuchi, M. Sano, A. Sumiyama, Y. Oda, H. Nagano, *Synth. Metals* **12**, 341–346 (1985)
16. I.T. Belash, A.D. Bronnikov, O.V. Zharikov, A.V. Pal'nichenko, *Solid State Commun.* **69**, 921–923 (1989)
17. I.T. Belash, A.D. Bronnikov, O.V. Zharikov, A.V. Pal'nichenko, *Synth. Met.* **36**, 283–302 (1990)
18. V.V. Avdeev, O.V. Zharikov, V.A. Nalimova, A.V. Pal'nichenko, K.N. Semenenko, *Pis'ma Zh. Eksp. Teor. Fiz.* **43**, 376–378 (1986)
19. L.A. Pendry, R. Wachnik, F.L. Vogel, P. Lagrange, G. Furdin, M.E. Makrini, A. Hérold, *Solid State Commun.* **38**, 677–681 (1981)
20. R.A. Wachnik, L.A. Pendry, F.L. Vogel, P. Lagrange, *Solid State Commun.* **43**, 5–8 (1982)
21. P. Lagrange, A. Bendriss-Rerhraya, J.F. Mareche, E. McRae, *Synth. Met.* **12**, 201–206 (1985)
22. A.F. Hebard, M.J. Rosseinsky, R.C. Haddon, D.W. Murphy, S.H. Glarum, T.T.M. Palstra, A.P. Ramirez, A.R. Kortan, *Nature* **350**, 600–601 (1991)
23. A. Gauzzi, S. Takashima, N. Takeshita, C. Terakura, H. Takagi, N. Emery, C. Hérold, P. Lagrange, G. Loupiau, *Phys. Rev. Lett.* **98**, 067002 (2007)
24. J.S. Kim, L. Boeri, J.R. O'Brien, F.S. Razavi, R.K. Kremer, *Phys. Rev. Lett.* **99**, 027001 (2007)
25. N. Emery, C. Hérold, J.F. Maréché, C. Bellouard, G. Loupiau, P. Lagrange, *J. Solid State Chem.* **179**, 1289–1292 (2006)
26. D. Guerard, M. Chaabouni, P. Lagrange, M.E. Makrini, A. Hérold, *Carbon* **18**, 257–264 (1980)
27. R.P. Smith, A. Kusmartseva, Y.T.C. Ko, S.S. Saxena, A. Akrap, L. Forró, M. Laad, T.E. Weller, M. Ellerby, N.T. Skipper, *Phys. Rev. B* **74**, 024505 (2006)
28. L.E. DeLong, V. Yeh, V. Tondiglia, P.C. Eklund, S.E. Lambert, M.B. Maple, *Phys. Rev. B* **26**, 6315–6318 (1982)
29. H. Okazaki, R. Yoshida, K. Iwai, K. Noami, T. Muro, T. Nakamura, T. Wakita, Y. Muraoka, M. Hirai, F. Tomioka, Y. Takano, A. Takenaka, M. Toyoda, T. Oguchi, T. Yokoya, *Phys. Rev. B* **80**, 035420 (2009)
30. G. Csányi, P.B. Littlewood, A.H. Nevidomsky, C.J. Pickard, B.D. Simons, *Nat. Phys.* **1**, 42–45 (2005)
31. M. Calandra, F. Mauri, *Phys. Rev. Lett.* **95**, 237002 (2005)
32. D.G. Hinks, D. Rosenmann, H. Claus, M.S. Bailey, J.D. Jorgensen, *Phys. Rev. B* **75**, 014509 (2007)
33. J. Bardeen, L. Cooper, J.R. Schrieffer, *Phys. Rev.* **108**, 1175 (1957)
34. G. Lamura, M. Aurino, G. Cifariello, E.D. Gennaro, A. Andreone, N. Emery, C. Hérold, J.F. Maréché, P. Lagrange, *Phys. Rev. Lett.* **96**, 107008 (2006)
35. J.S. Kim, R.K. Kremer, L. Boeri, F.S. Razavi, *Phys. Rev. Lett.* **96**, 217002 (2006)
36. N. Bergeal, V. Dubost, Y. Noat, W. Sacks, D. Roditchev, N. Emery, C. Hérold, J.-F. Maréché, P. Lagrange, G. Loupiau, *Phys. Rev. Lett.* **97**, 077003 (2006)
37. A. Sanna, G. Profeta, A. Floris, A. Marini, E.K.U. Gross, S. Massidda, *Phys. Rev. B* **75**, 020511(R) (2007)
38. R.S. Gonnelli, D. Daghero, D. Delaude, M. Tortello, G.A. Umbarino, V.A. Stepanov, J.S. Kim, R.K. Kremer, A. Sanna, G. Profeta, S. Massidda, *Phys. Rev. Lett.* **100**, 207004 (2008)
39. R.J. Baird, C.S. Fadley, L.F. Wagner, *Phys. Rev. B* **15**, 666 (1977)
40. S. Takahashi, S. Kono, H. Sakurai, T. Sagawa, *J. Phys. Soc. Jpn.* **51**, 3296 (1982)
41. W.F. Egelhoff Jr., *Phys. Rev. B* **30**, 1052 (1984)

42. T. Matsushita, F. Matsui, *J. Electron Spectrosc. Relat. Phenom.* **195**, 365–374 (2014)
43. F. Matsui, H. Nishikawa, H. Daimon, M. Muntwiler, M. Takizawa, H. Namba, T. Greber, *Phys. Rev. B* **97**, 045430 (2018)
44. F. Matsui, T. Matsushita, H. Daimon, *J. Phys. Soc. Jpn.* **81**, 114604 (2012)
45. F. Matsui, R. Ishii, H. Matsuda, M. Morita, S. Kitagawa, T. Matsushita, S. Koh, H. Daimon, *Jpn. J. Appl. Phys.* **52**, 110110 (2013)
46. F. Matsui, R. Eguchi, S. Nishiyama, M. Izumi, E. Uesugi, H. Goto, T. Matsushita, K. Sugita, H. Daimon, Y. Hamamoto, I. Hamada, Y. Morikawa, Y. Kubozono, *Sci. Rep.* **6**, 36258 (2016)
47. T. Uchihashi, P. Mishra, M. Aono, T. Nakamura, *Phys. Rev. Lett.* **107**, 207001 (2011)
48. T. Zhang, P. Cheng, W.-J. Li, Y.-J. Sun, G. Wang, X.-G. Zhu, K. He, L. Wang, X. Ma, X. Chen, Y. Wang, Y. Liu, H.-Q. Lin, J.-F. Jie, Q.-K. Xue, *Nat. Phys.* **6**, 104–108 (2010)
49. J.-F. Ge, Z.-L. Lie, C. Liu, C.-L. Gao, D. Qian, Q.-K. Xue, Y. Liu, J.-F. Jia, *Nat. Mater.* **14**, 285–289 (2015)
50. M. Yano, A. Sekiyama, H. Fujiwara, T. Saita, S. Imada, T. Muro, Y. Onuki, S. Suga, *Phys. Rev. Lett.* **98**, 036405 (2007)
51. A. Sekiyama, T. Iwasaki, K. Matsuda, Y. Saitoh, Y. Onuki, S. Suga, *Nature* **403**, 396 (2000)
52. K. Horiba, M. Taguchi, A. Chainani, Y. Takata, E. Ikenaga, D. Miwa, Y. Nishino, K. Tamasaku, M. Awaji, A. Takeuchi, M. Yabashi, H. Namatame, M. Taniguchi, H. Kumigashira, M. Oshima, M. Lippmaa, M. Kawasaki, H. Koinuma, K. Kobayashi, T. Ishikawa, S. Shin, *Phys. Rev. Lett.* **93**, 236401 (2004)
53. Y. Takata, K. Tamawaku, T. Tokushima, D. Miwa, S. Shin, T. Ishikawa, M. Yabashi, K. Kobayashi, J.J. Kim, T. Yao, T. Yamamoto, *Appl. Phys. Lett.* **84**, 4310 (2004)
54. S.M. Golberg, C.S. Fadley, S. Kono, *J. Electron Spectrosc. Relat. Phenom.* **21**, 285 (1981)
55. H. Daimon, S. Imada, H. Nishimoto, S. Suga, *J. Electron Spectrosc. Relat. Phenom.* **76**, 487 (1995)
56. H. Nishimoto, T. Nakatani, T. Matsushita, S. Imada, H. Daimon, S. Suga, *J. Phys. Condens. Matter* **8**, 2715 (1996)
57. F. Matsui, Y. Hori, H. Miyata, N. Suganuma, H. Daimon, H. Totsuka, K. Ogawa, T. Furukubo, H. Namba, *Appl. Phys. Lett.* **81**, 2556 (2002)
58. T. Valla, J. Camacho, Z.-H. Pan, A.V. Fedorov, A.C. Walters, C.A. Howard, M. Ellerby, *Phys. Rev. Lett.* **102**, 107007 (2009)
59. K. Sugawara, T. Sato, T. Takahashi, *Nat. Phys.* **5**, 40–43 (2009)
60. S.-L. Yang, J.A. Sobota, C.A. Howard, C.J. Pickard, M. Hashimoto, D.H. Lu, S.-K. Mo, P.S. Kirchmann, Z.-X. Shen, *Nat. Commun.* **5**, 3493 (2014)
61. Y. Kubozono, R. Eguchi, H. Goto, S. Hamao, T. Kambe, T. Terao, S. Nishiyama, L. Zheng, X. Miao, H. Okamoto, *J. Phys. Condens. Matter* **28**, 334001 (2016)